



# Hollow sphere of heterojunction (NiCu)S/NC as advanced anode for sodium-ion battery

Hongyi Chen, Pengfei Lv, Pengfu Tian, Shiyue Cao, Shengjun Yuan, Qiming Liu \*

Key Laboratory of Artificial Micro- and Nano-structures of Ministry of Education, School of Physics and Technology, Wuhan University, Wuhan 430072, Hubei, China

## ARTICLE INFO

### Article history:

Received 10 February 2023

Revised 8 March 2023

Accepted 11 March 2023

Available online 27 March 2023

### Keywords:

Hollow structure

Heterogeneous interface

First principle calculations

Sodium-ion batteries

## ABSTRACT

Metal sulfide is considered as a potential anode for sodium-ion batteries (SIBs), due to the high theoretical capacity, strong thermodynamic stability and low-cost. However, their cycle capacity and rate performance are limited by the excessive expansion rate and low intrinsic conductivity. Herein, heterogeneous hollow sphere NiS-Cu<sub>9</sub>S<sub>5</sub>/NC (labeled as (NiCu)S/NC) based on Oswald ripening mechanism was prepared through a simple and feasible methodology. From a structural perspective, the hollow structure provides an expansion buffer and raises the electrochemical active area. In terms of electron/ion during the cycles, Na<sup>+</sup> storage mechanism is optimized by NiS/Cu<sub>9</sub>S<sub>5</sub> heterogeneous interface, which increases the storage sites and shortens the migration path of Na<sup>+</sup>. The formation of built-in electric field strengthens the electron/ion mobility. Based on the first principle calculations, it is further proved the formation of heterogeneous interfaces and the direction of electron flow. As the anode for SIBs, the synthesized (NiCu)S/NC delivers high reverse capacity (559.2 mA h g<sup>-1</sup> at 0.5 A g<sup>-1</sup>), outstanding rate performance (185.3 mA h g<sup>-1</sup> at 15 A g<sup>-1</sup>), long-durable stability (342.6 mA h g<sup>-1</sup> at 4 A g<sup>-1</sup> after 1500 cycles, 150.0 mA h g<sup>-1</sup> at 10 A g<sup>-1</sup> after 20,000 cycles with 0.0025% average attenuation rate). The matching cathode electrode Na<sub>3</sub>V<sub>2</sub>(PO<sub>4</sub>)<sub>3</sub>/C is assembled with (NiCu)S/NC for the full-battery that achieves high energy density (253.7 W h kg<sup>-1</sup>) and reverse capacity (288.7 mA h g<sup>-1</sup>). The present work provides a distinctive strategy for constructing electrodes with excellent capacity and stability for SIBs.

© 2023 Science Press and Dalian Institute of Chemical Physics, Chinese Academy of Sciences. Published by ELSEVIER B.V. and Science Press. All rights reserved.

## 1. Introduction

The problem of energy is the shackle that restricts the development of human civilization and society [1,2]. The progress of energy technology can not only promote the advancement of technology but also empower the economy [3,4]. Lithium-ion batteries (LIBs) are widely used in our daily life as highly efficient energy conversion devices [5]. However, the surge in prices of lithium resources caused by resources shortages limits its further development in the future [6–8]. Sodium-ion batteries (SIBs), which possess the same “rocking chair” charge/discharge mechanism as LIBs, have been widely studied because of the low cost and wide distribution of sodium resources [9–11]. In addition to the cost advantage, SIBs also have unique advantages compared to LIBs, such as high security and better high/low temperature performance [12–14]. Nevertheless, Na<sup>+</sup> with larger radius than Li<sup>+</sup> cannot make the energy density and volume density of SIBs reach the level of LIBs, mainly caused by the inappropriate electrode

material [15]. Therefore, it is crucial to search for a suitable electrode material for SIBs.

Transition metal sulfides can be alternative anodes for SIBs because of multi-space structure, high theoretical capacity, and various Na<sup>+</sup> storage mechanisms [16,17]. The metal–S bond has a lower bond energy than metal–O bond, which lowers the barrier potential in the process of sodiation/desodiation [18]. NiS, as the representative transition metal sulfide, has high theoretical sodium storage capacity, strong thermodynamic stability, economical cost, and relatively easy experimental preparation method [19–21]. However, the high expansion rate of converted-type NiS makes it easy to be pulverized during the charge/discharge process [22]. The problem of inherent low conductivity also restricts the rate performance of NiS [23]. The structural deformation in the converse reaction makes the actual sodium storage capacity of NiS far less than its theoretical capacity [24,25]. The key to optimize the electrochemical performance of NiS is to restrain its volume expansion and improve its conductivity.

Focusing on the above problems, the construction of hollow bimetallic sulfide heterojunction is considered as an effective approach to enhance the electrochemical performance of NiS. From

\* Corresponding author.

E-mail address: [qmliu@whu.edu.cn](mailto:qmliu@whu.edu.cn) (Q. Liu).

the structural perspective, the proper hollow structure alleviates the volume expansion during the cycles and increases the contact area with the electrolyte [26,27]. Fan et al. designed a multi-shelled hollow sphere of NiS for the anode of SIBs, which attained the capacity of 531.5 mA h g<sup>-1</sup> at 0.05 A g<sup>-1</sup> [28]. While from the molecule perspective, the formation of built-in electric field induced by heterogeneous parts accelerates the electron/ion transport mobility [29]. Heterogeneous interfaces improve Na<sup>+</sup> storage mechanism by providing plenty of storage sites [30]. The interface shortens the ion diffusion pathway and reduces the damage of electrode structure. Heterogeneous bimetallic sulfide NiS/MoS<sub>2</sub>/C was prepared by Xie et al. and reached the capacity of 516 mA h g<sup>-1</sup> at 0.1 A g<sup>-1</sup> [31]. He et al. synthesized NiS<sub>2</sub>/NiSe<sub>2</sub> hetero-structure that delivered high rate capacity of 353 mA h g<sup>-1</sup> at 5.0 A g<sup>-1</sup> [32]. There are few reports on the construction of heterogeneous hollow structures to improve the electrochemical performance of SIB electrodes. There are four important reasons for selecting NiS-Cu<sub>9</sub>S<sub>5</sub> heterogeneous hollow structure: (1) NiS and Cu<sub>9</sub>S<sub>5</sub> electrodes both have the capacity to store sodium ions; (2) because they are sulfides, NiS-Cu<sub>9</sub>S<sub>5</sub> hetero-structure is easy to prepare; (3) different work functions of NiS and Cu<sub>9</sub>S<sub>5</sub> are the basis for forming heterojunctions [33,34], and the specific values of work function are confirmed by the first principle calculations in our work; (4) the raw materials for synthesizing NiS and Cu<sub>9</sub>S<sub>5</sub> are low-cost, environment-friendly, and rich-reserves.

In this work, the hollow sphere of heterojunction NiS-Cu<sub>9</sub>S<sub>5</sub>/NC, labeled as (NiCu)S/NC, was prepared by one-step solvo-thermal and subsequent annealing treatment. Hollow structure based on the Oswald-ripening mechanism can alleviate the volume stress in the process of sodiation/desodiation and increase the effective active area. Heterogeneous interface of NiS/Cu<sub>9</sub>S<sub>5</sub> provides active sites for Na<sup>+</sup> and accelerates the migration rate of electron/ion. The formation of the built-in electric field accelerates carrier transport and improves electrical activity and conductivity. In addition, polyvinyl-pyrrolidone (PVP)-derived carbon is located on the matrix of micro-sphere, which is beneficial to the structural integrity of (NiCu)S/NC. Density functional theory (DFT) calculations prove that the NiS-Cu<sub>9</sub>S<sub>5</sub> heterojunction can increase the carrier concentration by forming the built-in electric field. As the anode for SIBs, (NiCu)S/NC delivers ultra-high discharge capacity (581.5 mA h g<sup>-1</sup>) and charge capacity (549.3 mA h g<sup>-1</sup>) with 94.46% initial Coulombic efficiency. It can retain reversible capacity of 342.6 mA h g<sup>-1</sup> with 81.6% capacity retention at 4 A g<sup>-1</sup> after 1500 cycles, much higher than NiS/NC (212.5 mA h g<sup>-1</sup>) and Cu<sub>9</sub>S<sub>5</sub>/NC (200.2 mA h g<sup>-1</sup>). And (NiCu)S/NC exhibits the reverse capacity of 185.3 mA h g<sup>-1</sup> at the high current density of 15 A g<sup>-1</sup>. After 20,000 cycles at 10 A g<sup>-1</sup>, the electrode still maintains the capacity of 150 mA h g<sup>-1</sup> with 0.0025% average attenuation rate and it only takes 87 s to charge fully. It is worth mentioning that (NiCu)S/NC-Na<sub>3</sub>V<sub>2</sub>(PO<sub>4</sub>)<sub>3</sub>/C full-battery shows a high energy density of 253.7 W h kg<sup>-1</sup> and reverse capacity of 288.7 mA h g<sup>-1</sup>. In this work, a novel hollow hetero-structure (NiCu)S/NC anode we prepared provides a new perspective to construct high capacity and stable electrodes for SIBs.

## 2. Experimental

### 2.1. The synthesis of (NiCu)S/NC

Firstly, 0.4 g PVP (*M<sub>w</sub>* = 58000) was added to the solvent of ethanediol and stirred until dissolved. Then (3 - *x*) mmol NiSO<sub>4</sub>·6H<sub>2</sub>O and *x* mmol CuCl<sub>2</sub>·2H<sub>2</sub>O were triturated and mixed in an agate mortar. The evenly mixed powder was added to the mixed solvent. After stirring for 30 min, 3 mmol ground sublimed sulfur (0.096 g) and 3 mmol thioureas (0.228 g) were added to the above

solution. The precipitated solution was added to Teflon liner, which was heated to 180 °C for 18 h. After cooling, the final product was washed successively by deionized water and alcohol, then put in an oven for 12 h. The sample was obtained after a carbonization treatment under Ar flow at 600 °C for 3 h with a heating rate of 5 °C min<sup>-1</sup>. In addition, samples with 6 and 12 h solvo-thermal reaction time were prepared to explore the growth process. When *x* is 0, 1.5, 2, 2.5, and 3, the products are labeled as NiS/NC, N-(NiCu)S/NC, (NiCu)S/NC, C-(NiCu)S/NC, and Cu<sub>9</sub>S<sub>5</sub>/NC.

### 2.2. The synthesis of Na<sub>3</sub>V<sub>2</sub>(PO<sub>4</sub>)<sub>3</sub>/C

The Na<sub>3</sub>V<sub>2</sub>(PO<sub>4</sub>)<sub>3</sub>/C was prepared by using our previous method [35].

### 2.3. Characterization of materials

X-ray diffraction (XRD, Bruker D8 advance, Cu K<sub>α</sub> radiation) was employed to identify material types and crystal orientations. Valence states of elements of samples were tested by X-ray photoelectron spectroscopy (XPS, Al K<sub>α</sub> radiation, USA). Morphological and structural characterizations were detected by scanning electron microscope (SEM) (Zeiss GeminiSEM 500) and transmission electron microscope (TEM) (JEM-2010 HT and JEM-F200). Inductively coupled plasma-atomic emission spectroscopy (ICP-AES, IRIS Intrepid II XSP) was used to confirm the elemental content. The carbon structure was explored by SEM with Raman attachment. The thermogravimetric analysis (TGA, A NETZSCH STA 449C) with a heating speed of 5 °C min<sup>-1</sup> in air was utilized to analyze the content of carbon.

### 2.4. Electrochemical measurements

A series of 2032-type coin cells were prepared to explore the electrochemical performances of as-prepared samples. Firstly, active material (60%), carbon black (20%), polymerized styrene butadiene rubber (SBR, 10%), and carboxymethyl cellulose (CMC, 10%) were mixed with deionized water to form a uniform slurry. The slurry was spread on the copper foil as current collector (Al foil was used as current collector only when cathode was Na<sub>3</sub>V<sub>2</sub>(PO<sub>4</sub>)<sub>3</sub>/C). After drying in a vacuum oven for 12 h, the copper foil covered with the slurry was tailored to 12 mm discs with an active material load of 1–1.5 mg. Lastly, the electrodes, counter electrode, electrolyte (120 μL 1 M sodium hexafluorophosphate (NaPF<sub>6</sub>) in diglyme (DGM)), separator (Whatman GF/A), and fittings were assembled into coin cells in a glove box. Specifically, the counter electrodes in half and full batteries were metallic sodium and Na<sub>3</sub>V<sub>2</sub>(PO<sub>4</sub>)<sub>3</sub>/C, respectively. All as-prepare batteries stand for 8 h to be saturated completely with the electrolyte. Land battery testing system (LANHE-CT2001) was employed to measure the cyclic capacity, rate performance, and quick charge ability. Cyclic voltammogram (CV, 0.5 to 2.5 mV s<sup>-1</sup>) curves and electrochemical impedance spectroscopy (EIS, 0.01 Hz to 100 kHz) plots were tested by electrochemical workstation (CHI 760E, Shanghai Chenhua, China). The lower cut-off voltage was set at 0.2 V to exclude the Na<sup>+</sup> intercalation of carbon and the under-potential deposition of metallic sodium.

### 2.5. Computational details

All the first-principles calculations were performed using the projector augmented wave (PAW) method [36] as implemented in the Vienna Ab initio Simulation Package (VASP) code [37]. Generalized gradient approximation (GGA) in the form of Perdew-Burke-Ernzerhof (PBE) [36] was used as the exchange–correlation functional. The vdW-DF3 functional [38] that was proven to be a

good description of weak van der Waals interactions was also taken into consideration to correct the interactions between interfaces. The energy cutoff for plane-wave expansion and the width of smearing were set to 400 eV and 0.05 eV, respectively.

The interface supercell containing 208 atoms was composed of NiS (1 0 0) and  $\text{Cu}_9\text{S}_5$  (0 0 15) surfaces. The model for NiS,  $\text{Cu}_9\text{S}_5$ , and NiS- $\text{Cu}_9\text{S}_5$  interface was fully optimized. The Monkhorst-Pack scheme [39]  $k$ -point grid of  $(1 \times 1 \times 1)$  was used for relaxation and a grid of  $(2 \times 5 \times 1)$  was used for self-consistent field calculations until the change of total energy is less than  $10^{-5}$  eV. A vacuum layer of 20 Å in thickness was introduced in  $z$  direction to avoid spurious interactions.

### 3. Results and discussion

The synthesis of hollow sphere of heterojunction (NiCu)S/NC is schematically shown in Fig. 1. After solvo-thermal treating for 6 h, the structure of (NiCu)S is a random aggregation of nano-spheres. As the reaction proceeds, the irregular aggregate transforms into a sphere. When the reaction continued for 18 h, the (NiCu)S solid sphere changed to hollow sphere. Lastly, the (NiCu)S/NC was obtained after a carbonization treatment under Ar flow at 600 °C for 3 h.

XRD patterns were employed to determine the material types and crystal forms. As shown in Fig. 2(a), the synthesized materials

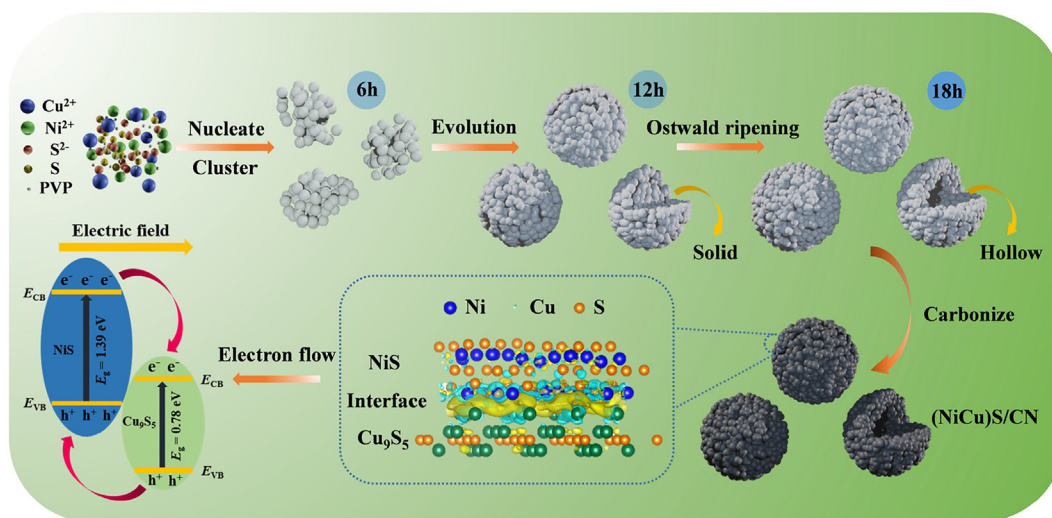


Fig. 1. Schematic illustration of the formation process of the (NiCu)S/NC.

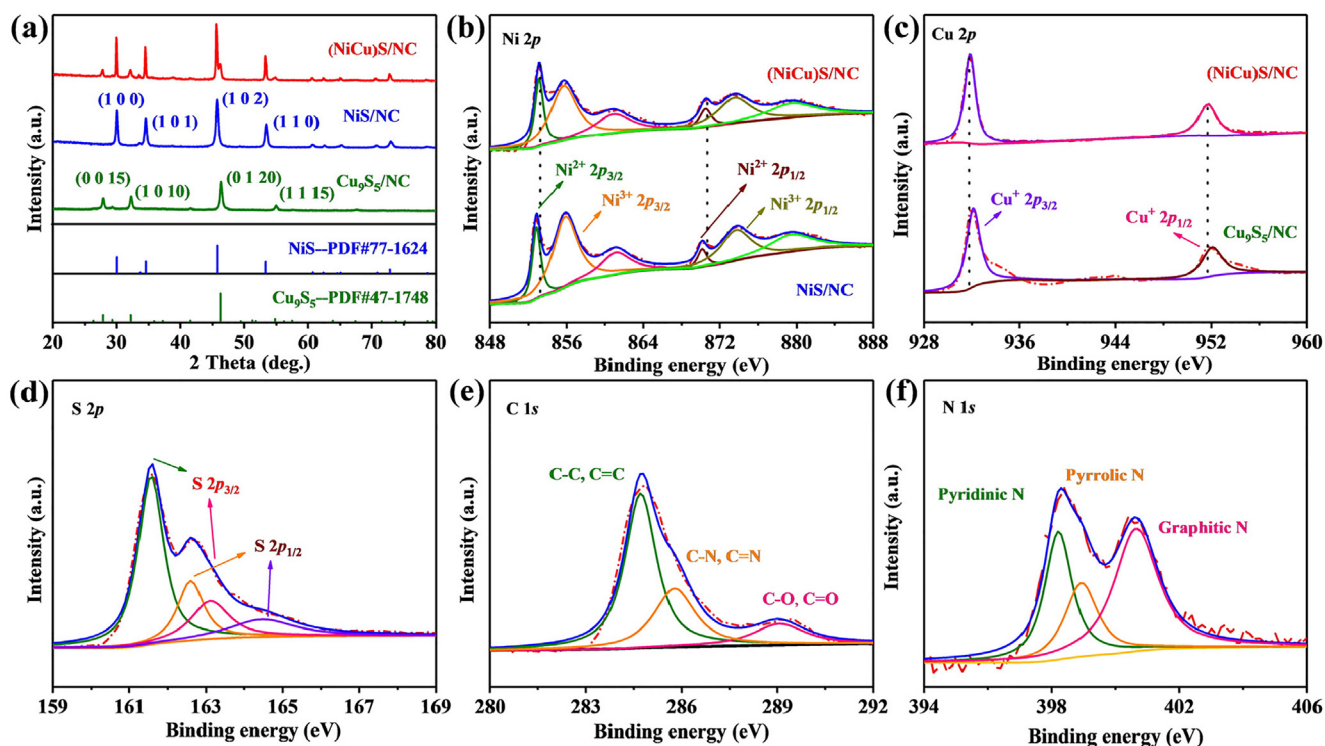
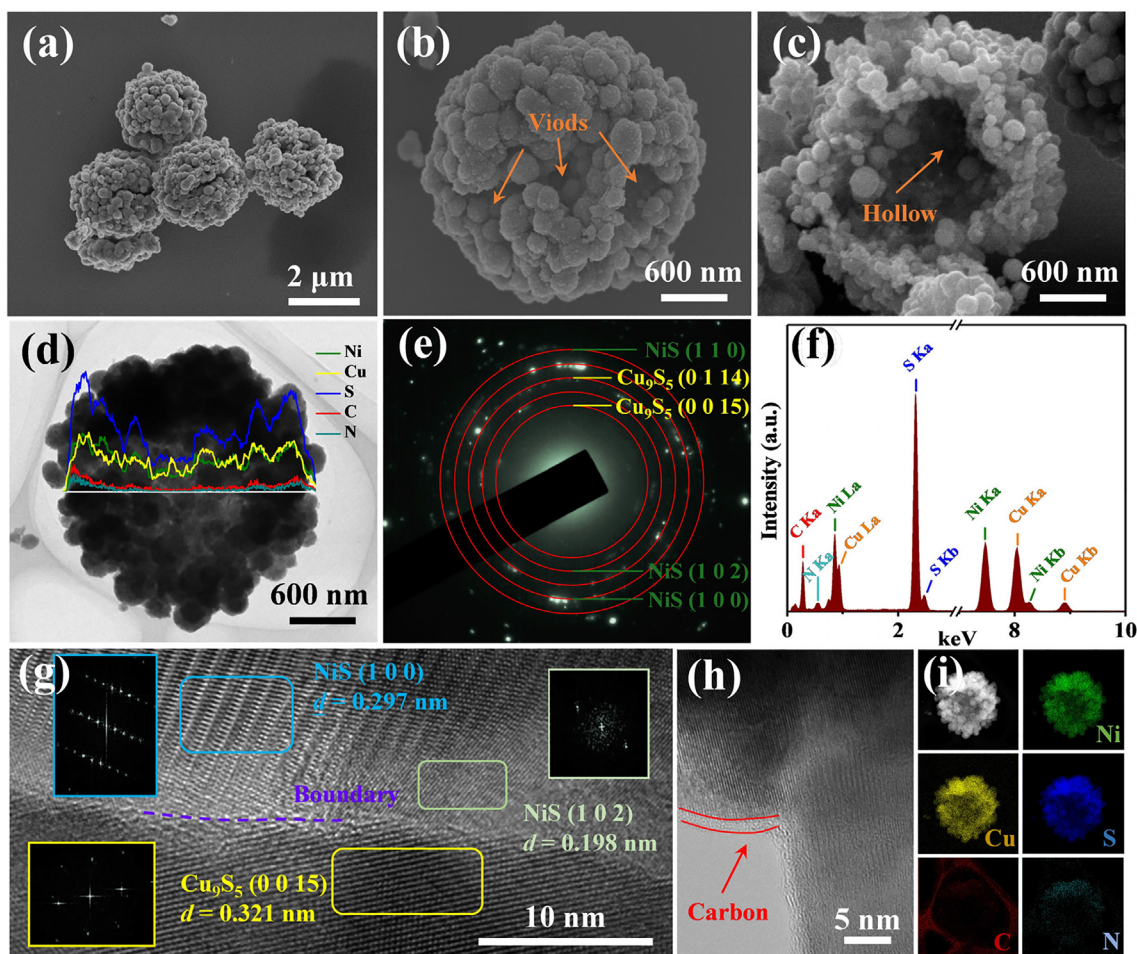


Fig. 2. Crystal and element valence detections. (a) XRD patterns of (NiCu)S/NC, NiS/NC, and  $\text{Cu}_9\text{S}_5$ /NC. XPS high-resolution spectra of (b) Ni 2p, (c) Cu 2p, (d) S 2p, (e) C 1s, and (f) N 1s.

were pure NiS (PDF#77-1624) or  $\text{Cu}_9\text{S}_5$  (PDF#47-1748) in the absence of  $\text{Ni}^{2+}$  or  $\text{Cu}^{2+}$ , respectively. The peaks of NiS and  $\text{Cu}_9\text{S}_5$  can be observed without impurity peaks in the XRD pattern of (NiCu)S/NC, which proves the successful preparation of heterogeneous compound of (NiCu)S/NC. The valence states of element were detected by XPS. As seen from Fig. S1, characteristic peaks of Ni, Cu, S, C, and N can be observed in full XPS spectrum. To verify the formation of heterojunction, the Ni 2p spectra of (NiCu)S/NC and NiS as well as the Cu 2p spectra of (NiCu)S/NC and  $\text{Cu}_9\text{S}_5$  were tested to confirm the electron flow direction. After building the compound of (NiCu)S/NC, the electron bonding energy of Ni 2p increases, indicating a decrease in the electron cloud density in the part of NiS (Fig. 2b) [40,41]. The opposite happens to Cu 2p, which shows an influx of electrons in  $\text{Cu}_9\text{S}_5$  (Fig. 2c). Generally, the formation of the built-in electric field induced by heterojunction causes the electrons in NiS to flow to  $\text{Cu}_9\text{S}_5$ . In terms of electronegativity, Ni-S has a weaker bond energy than Cu-S, and Cu atom has a stronger electron affinity than Ni-atom. High-resolution spectra of S 2p are split into four peaks at 161.6, 162.6, 163.1, and 164.5 eV, originating from the chemical bonds of Ni-S and Cu-S (Fig. 2d) [42]. In the C 1s core level spectra (Fig. 2e), the appearance of the three peaks indicates the formation of C-C/C=C, C-N/C=N, and C-O/C=O [43]. The carbon in the (NiCu)S/NC matrix effectively improves the electrical conductivity and reduces the volume expansion during the charge/discharge process. N 1s core level spectrum can be resolved into three peaks at 398.2, 398.9, and 400.6 eV, deriving from the pyridinic, pyrrolic,

and graphitic N [44,45]. N is located in carbon in the form of doping, which brings defects to carbon and further enhances the conductivity.

To explore (NiCu)S/NC from the perspective of nanoscale, SEM and TEM were employed to investigate the morphology and structure of (NiCu)S/NC. As shown in Fig. 3(a) and Fig. S2, the structure of (NiCu)S/NC is a hollow micro-sphere with a diameter of 2  $\mu\text{m}$ , which is composed of the nano-spheres with a diameter of 100–200 nm. By observing the SEM images of NiS/NC and  $\text{Cu}_9\text{S}_5$ /NC, NiS/NC is an individual sphere (100–200 nm) and does not aggregate into a large sphere (Fig. S3). While  $\text{Cu}_9\text{S}_5$ /NC is a self-assembled nano-flower structure. The nano-sphere structure of (NiCu)S/NC may inherit the structure of NiS/NC. Assembly characteristic from nano-sphere to micro-sphere may be derived from the structure of  $\text{Cu}_9\text{S}_5$ /NC. Micro-sphere of (NiCu)S/NC has many voids on the surface, which increases the electrolyte contact area and enhances the sodium storage (Fig. 3b). The hollow structure of (NiCu)S/NC alleviates the volume expansion during the cycling process and increases the effective electrochemical reaction area (Fig. 3c). The reason for the formation of the hollow structure is shown in Fig. 4. TEM images and linear scan element distribution further confirm the hollow structure and secondary component of (NiCu)S/NC (Fig. 3d). Selected area electron diffraction (SAED) is exhibited in Fig. 3(e), which includes the polycrystalline rings of NiS (corresponding to crystal face of (1 1 0), (1 0 2), and (1 0 0)) and  $\text{Cu}_9\text{S}_5$ /NC (corresponding to crystal face of (0 0 15) and (0 1 14)). ICP-AES and energy dispersive spectrometer (EDS) were



**Fig. 3.** Morphological and structural characterizations. (a–c) SEM images of (NiCu)S/NC under different magnifications. (d, h) TEM, (e) SAED, and (f) element content images of (NiCu)S/NC. (g) High-resolution TEM images and the regional Fourier transform of the lattice fringes of (NiCu)S/NC. (i) EDS mapping of single particles of (NiCu)S/NC.

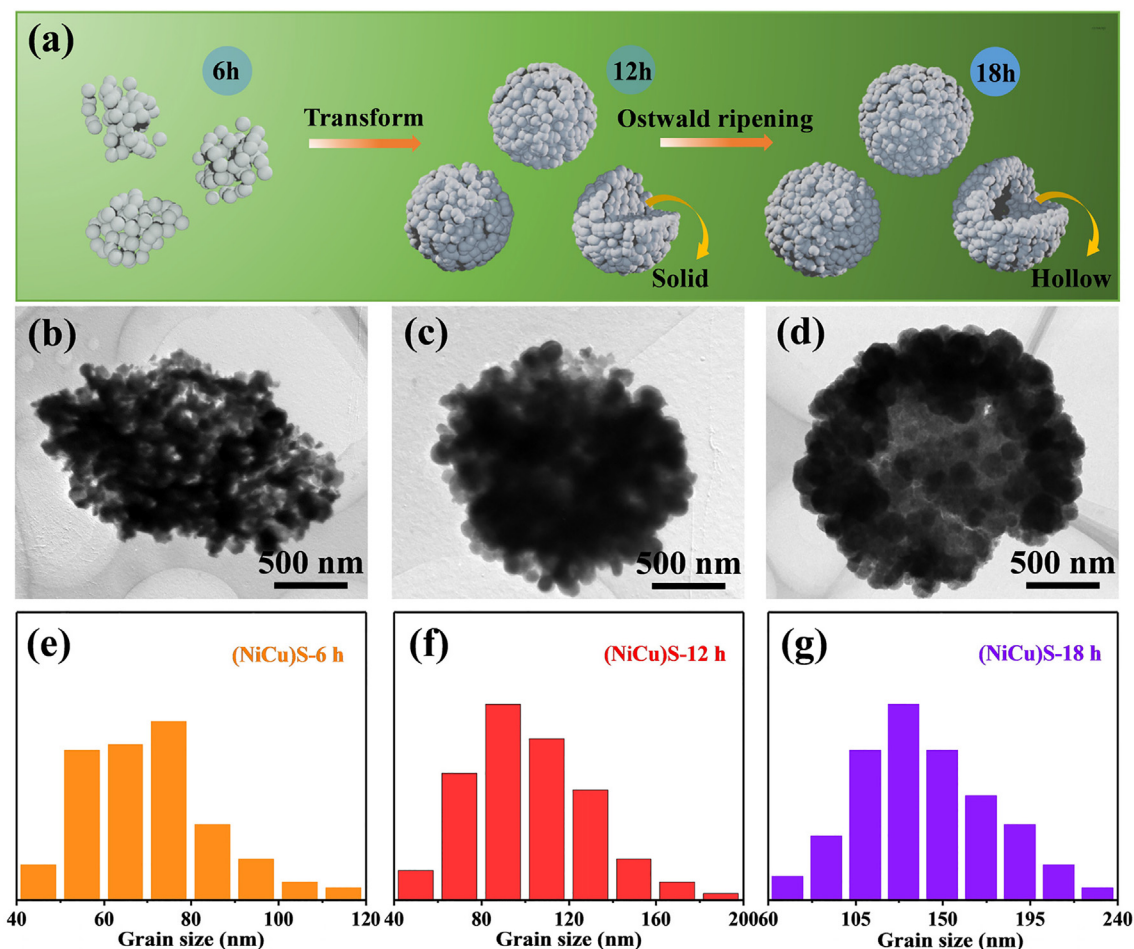


**Fig. 4.** Process of growth for hollow sphere. (a) Diagram of the formation of the hollow structure. TEM images and size distributions of (b, e) 6 h, (c, f) 12 h, and (d, g) 18 h solvo-thermal reaction of (NiCu)S.

used to determine the elemental content. EDS and ICP results are shown in Table S1, proving that atomic ratio of Ni to Cu in the (NiCu)S/NC is approximately 1:1. The ICP test, which is more sensitive to non-metallic elements (S), was chosen to prove the chemical formula. The atomic ratio results of ICP are basically consistent with the crystal structure in XRD, and the chemical formula is  $(\text{NiS}-1.04\text{Cu}_9\text{S}_5)/\text{NC}$  (Fig. 3f and Table S1). The content of N-doped carbon (NC) can be deduced by the TGA curves in Fig. S4. The weight loss in TGA curve is divided into two states. The weight loss between 0 and 300 °C can be attributed to the loss of water. According to the literature [46,47], the products of NiS,  $\text{Cu}_9\text{S}_5$ , and carbon at 800 °C are NiO, CuO, and  $\text{CO}_2$ , respectively. On the basis on the chemical formula of  $(\text{NiS}-1.04\text{Cu}_9\text{S}_5)/\text{NC}$ , the content of NC can be calculated as 4.56 wt%. To confirm the existence of heterojunction, high-resolution TEM was carried out to distinguish the grain types in different regions (Fig. 3g). Three different lattice spacing regions correspond to different material crystal surfaces. The lattice spacings of 0.297 and 0.198 nm are from the (1 0 0) and (1 0 2) planes of NiS. And the lattice spacing of 0.321 nm comes from the (0 0 15) plane of  $\text{Cu}_9\text{S}_5$ . An obvious crystal boundary between NiS and  $\text{Cu}_9\text{S}_5$  indicates that heterogeneous structure of NiS- $\text{Cu}_9\text{S}_5$  is successfully constructed. A heterogeneous interface provides more active sites for electron/ion and shortens carrier migration path. Fig. 3(h) shows the warp of N-doped carbon around the outside of the nano-sphere, which is beneficial to stabilize the structure of (NiCu)S/NC during the cycles. The signals of Ni, Cu, S, C, and N can be detected in EDS mapping, suggesting that the elements are uniformly distributed without aggregation (Fig. 3i).

To explore the formation process of hollow sphere of (NiCu)S, the TEM images and size distributions of different solvo-thermal times without the annealing process are employed to identify the structure of the different stages. When treated for 6 h, the structure of (NiCu)S is a random aggregation of nano-spheres (Fig. 4b and Fig. S5). Differing from the dispersive morphology of NiS, the aggregation may be caused by the self-assembly property of  $\text{Cu}_9\text{S}_5$ . As the reaction proceeds, the irregular aggregate transforms into a sphere (Fig. 4c and Fig. S5). Due to the high viscosity of ethylene glycol solvent, the same pressure is maintained in all parts of the solvent. Compared with sheet, rod-like, and other structures, spherical structure has the minimum surface area to maintain the smallest surface energy under the same volume. When the reaction lasted for 18 h, the (NiCu)S solid sphere changed to hollow sphere (Fig. 4d). According to the Ostwald ripening process, the energy inside the sphere is higher than outside [26,48]. With the nano-sphere growing, the difference between the inner and the outer energy becomes larger. The higher energy causes the inner particles to dissolve and the external particles to grow, resulting in the formation of hollow structures. The analysis of the particle size of different stages is displayed in Fig. 4(e-g). The nano-spheres, which form micro-sphere of (NiCu)S, continuously grow from 70 (6 h) to 130 nm (18 h). This result demonstrates the continued growth of small particles and supports the Ostwald ripening process. The corresponding schematic diagram of the growth process is shown in Fig. 4(a).

Na-(NiCu)S/NC, Na-NiS/NC, and Na- $\text{Cu}_9\text{S}_5$ /NC half-batteries were produced to explore their electrochemical properties. Fig. 5

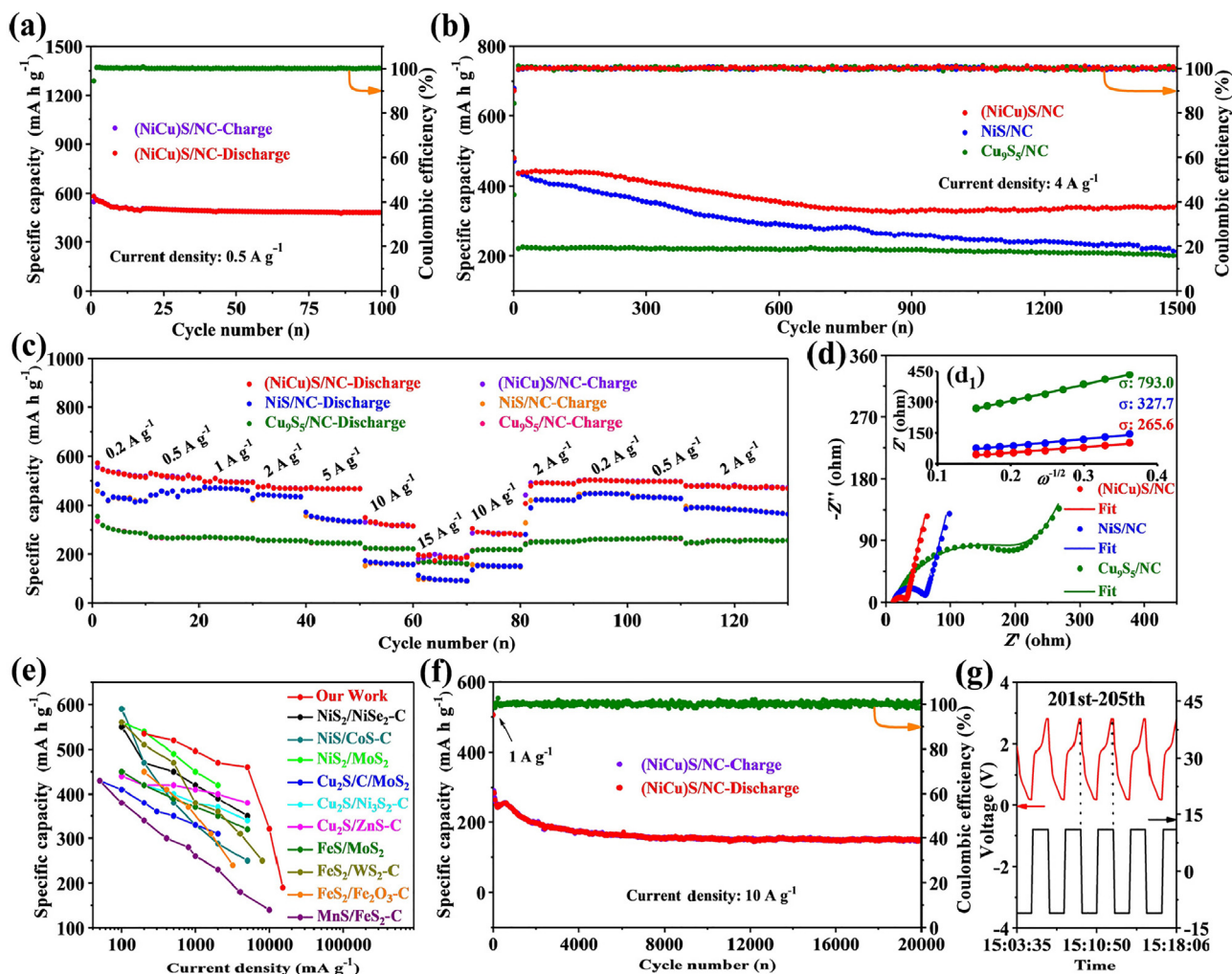


**Fig. 5.** Sodium storage capacities for half-battery. (a) Cyclic performance of (NiCu)S/NC at small current density ( $0.5 \text{ A g}^{-1}$ ). (b) Capacity comparison of (NiCu)S/NC, NiS/NC, and  $\text{Cu}_9\text{S}_5/\text{NC}$  at  $4 \text{ A g}^{-1}$ . (c) Rate performances at different current densities from  $0.2$  to  $15 \text{ A g}^{-1}$  and (d) Nyquist plots of (NiCu)S/NC, NiS/NC, and  $\text{Cu}_9\text{S}_5/\text{NC}$  (d1: fitting linear of  $Z''\text{-}\omega^{-1/2}$ ). (e) Comparison of rate performances of the reported compounds with (NiCu)S/NC. (f) Long-term durability cyclic performance and (g) relationship between voltage, current and time of (NiCu)S/NC at big current density ( $10 \text{ A g}^{-1}$ ).

(a) displays the cyclic performance of (NiCu)S/NC under small current density ( $0.5 \text{ A g}^{-1}$ ), which delivers high initial discharge capacity ( $581.5 \text{ mA h g}^{-1}$ ) and charge capacity ( $549.3 \text{ mA h g}^{-1}$ ) with 94.46% initial Coulombic efficiency (ICE). After establishing the solid electrolyte interface (SEI) in the first cycle, Coulombic efficiency (CE) quickly increases to 100%, suggesting that subsequent reactions are highly reversible. After 100 cycles at  $0.5 \text{ A g}^{-1}$ , (NiCu)S/NC electrode remains reversible capacity (stable capacity after cycles) of  $483.1 \text{ mA h g}^{-1}$ , and a slight attenuation in capacity is attributed to side effects. Fig. 5(b) exhibits the different electrochemical performances of (NiCu)S/NC, NiS/NC, and  $\text{Cu}_9\text{S}_5/\text{NC}$ . (NiCu)S/NC maintains reversible capacity of  $342.6 \text{ mA h g}^{-1}$  with 81.6% capacity retention at  $4 \text{ A g}^{-1}$  after 1500 cycles, much higher than NiS/NC ( $212.5 \text{ mA h g}^{-1}$ ) and  $\text{Cu}_9\text{S}_5/\text{NC}$  ( $200.2 \text{ mA h g}^{-1}$ ). Through the half-batteries test, (NiCu)S/NC has both the advantages of high capacity of NiS/NC and high stability of  $\text{Cu}_9\text{S}_5/\text{NC}$ , which is induced by the heterogeneous hollow structure. Specifically, the heterogeneous interfaces provide plenty of point defects, dislocations, and crystal boundaries, which can enhance the storage capacity of  $\text{Na}^+$ . For NiS/NC or  $\text{Cu}_9\text{S}_5/\text{NC}$ ,  $\text{Na}^+$  can only store in a bulk phase. While for (NiCu)S/NC, there is extra abundant  $\text{Na}^+$  storage sites at heterogeneous interfaces. These  $\text{Na}^+$  ions stored in heterogeneous interfaces are more easily diffused in the

electrochemical reaction, and they reduce the structural damage during the cycles. The hollow spherical structure increases the contact area with the electrolyte and alleviates the spherical shell rupture caused by volume expansion. After 1500 cycles at  $4 \text{ A g}^{-1}$ , morphology and structure of (NiCu)S/NC remain basically intact (Fig. S6a and b), suggesting its excellent cyclic performance. The particles of NiS/NC are broken and aggregated (Fig. S6c). Galvanostatic charge-discharge curves of different cycles were employed to analyze the reason for capacity fading of (NiCu)S/NC and NiS/NC (Fig. S7). The capacity attenuation of (NiCu)S/NC and NiS/NC is due to the same voltage platform shortening, corresponding to the irreversible  $\text{Na}^+$  extraction/insertion in the bulk of NiS. (NiCu)S/NC with a heterogeneous hollow structure has a variety of sodium storage sites, which enhances its cycle stability.

Rate performances at various current densities (from  $0.2$  to  $15 \text{ A g}^{-1}$ ) of (NiCu)S/NC, NiS/NC, and  $\text{Cu}_9\text{S}_5/\text{NC}$  are displayed in Fig. 5(c). When the current densities are set to  $0.2, 0.5, 1, 2, 5, 10,$  and  $15 \text{ A g}^{-1}$ , (NiCu)S/NC shows the average capacities of  $529.3, 514.3, 495.6, 470.1, 467.3, 322.6,$  and  $185.3 \text{ mA h g}^{-1}$ , respectively. By contrast, the average capacities of NiS/NC only achieve  $431.2, 458.1, 468.5, 439.4, 342.9, 160.6,$  and  $95.1 \text{ mA h g}^{-1}$ , and  $\text{Cu}_9\text{S}_5/\text{NC}$  is  $296.3, 263.7, 263.8, 253.8, 243.9, 220.9,$  and  $165.4 \text{ mA h g}^{-1}$ . To prove the stability of the rate capacity of (NiCu)S/NC, a multi-

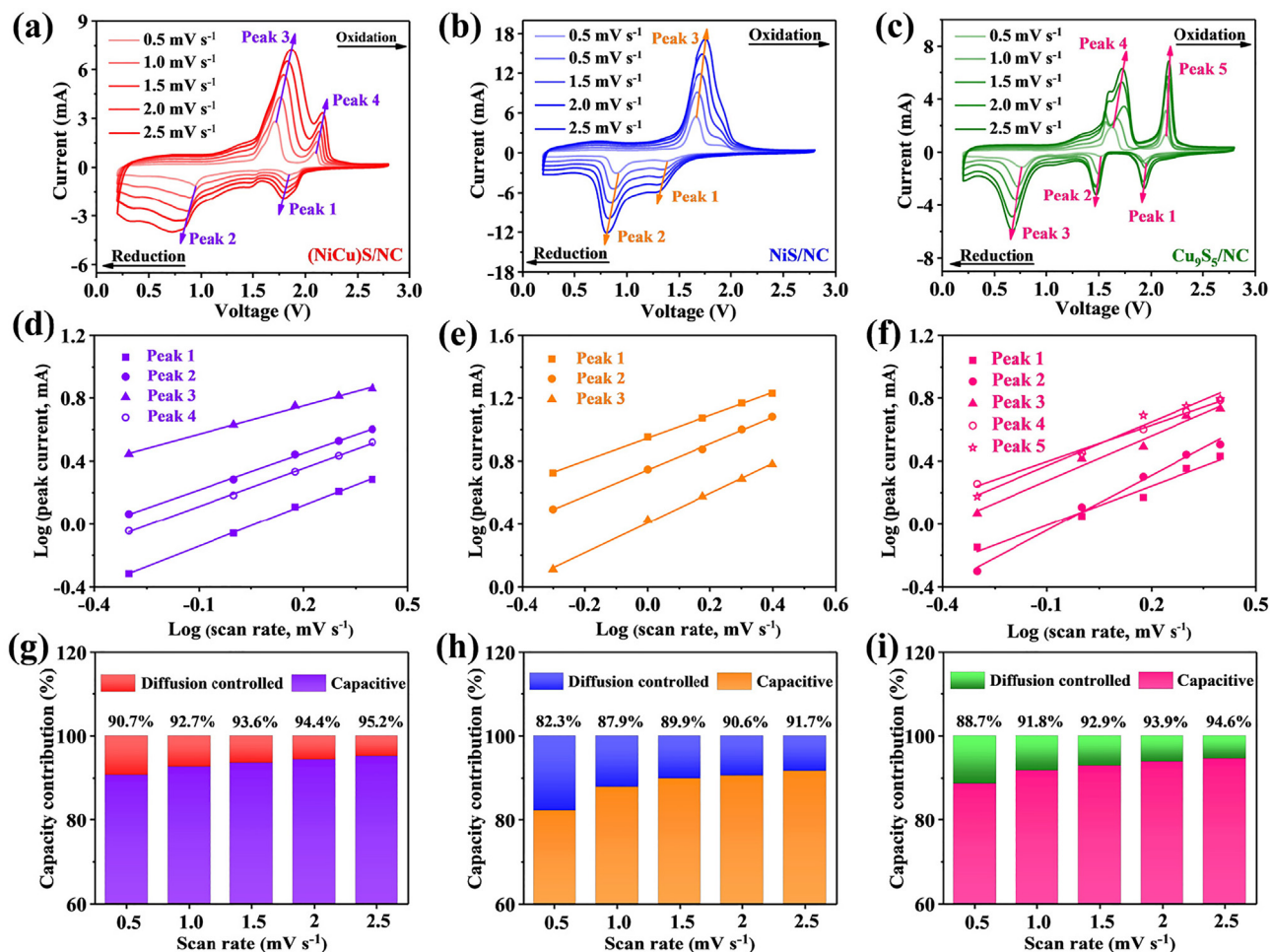


**Fig. 6.** Electrochemical kinetics mechanisms. CV profiles at different scan rates (from 0.5 to 2.5  $\text{mV s}^{-1}$ ) of (a) (NiCu)S/NC, (b) NiS/NC, and (c)  $\text{Cu}_9\text{S}_5/\text{NC}$ . The corresponding  $b$ -values of the redox peaks of (d) (NiCu)S/NC, (e) NiS/NC, and (f)  $\text{Cu}_9\text{S}_5/\text{NC}$ . Contribution ratio of pseudo-capacitance of (g) (NiCu)S/NC, (h) NiS/NC, and (i)  $\text{Cu}_9\text{S}_5/\text{NC}$ .

stage current recovery process is adopted. When the current densities recover to 10, 2, 0.2, and 0.5  $\text{A g}^{-1}$ , the reversible capacities of (NiCu)S/NC reach 286, 492, 502 and 497.3  $\text{mA h g}^{-1}$  with 88.7%, 104.7%, 94.8% and 96.7% capacity recovery, respectively. By coupling different components, a NiS- $\text{Cu}_9\text{S}_5$  heterogeneous structure with stable rate performance has been constructed. Due to the different work functions, a built-in electric field has been formed between the interface of NiS and  $\text{Cu}_9\text{S}_5$ , which accelerates the electron/ion transport rate and stabilizes the electrode structure. The Nyquist plots of (NiCu)S/NC, NiS/NC, and  $\text{Cu}_9\text{S}_5/\text{NC}$  are shown in Fig. 5(d). The EIS curve consists of a semicircle in the high-frequency and a straight line in the low-frequency, corresponding to the carrier transfer resistance at the interface ( $R_{\text{ct}}$ ) and the  $\text{Na}^+$  diffusion resistance in the electrode, respectively [26,49]. After equivalent circuit fitting, the  $R_{\text{ct}}$  value of (NiCu)S/NC is 19.6  $\Omega$ , much lower than that of NiS/NC (47.5  $\Omega$ ) and  $\text{Cu}_9\text{S}_5/\text{NC}$  (234.6  $\Omega$ ). The diffusion rate of  $\text{Na}^+$  inside the electrode can be determined by the following equations [50].

$$Z' = R + \sigma \omega^{-1/2} (\omega = 2\pi f) \quad (1)$$

$$D_{\text{Na}^+} = \frac{1}{2} R^2 T^2 A^{-2} n^{-4} F^{-4} C_{\text{Na}}^{-2} \sigma^{-2} \quad (2)$$

$R$ ,  $T$ ,  $A$ ,  $n$ ,  $F$  and  $C$  are constant in Eqs. (1) and (2).  $\sigma$  (Warburg factor) can be calculated from the relationship of  $Z'$  and  $\omega^{-1/2}$ . There is a negative correlation between of  $D_{\text{Na}^+}$  and  $\sigma$ . As displayed in the illustration (d1) of Fig. 5(d), the  $\sigma$  values of (NiCu)S/NC, NiS/

NC, and  $\text{Cu}_9\text{S}_5/\text{NC}$  are 265.6, 327.7, and 793.0  $\Omega$  respectively, delivering that (NiCu)S/NC electrode has the fastest  $\text{Na}^+$  diffusion rate. The enhancement of electronic and ionic conductance can support the built-in electric field theory, which improves the rate capability of (NiCu)S/NC. The comparison of the rate capacities between (NiCu)S/NC and other hetero-structural materials is displayed in Fig. 5(e) [25,32,43,51–57].

To verify the long cycles capacity retention and fast charging ability, 20,000 cycles at 10  $\text{A g}^{-1}$  high current density were carried out for (NiCu)S/NC anode. As a result, (NiCu)S/NC electrode exhibits a residual capacity of 150  $\text{mA h g}^{-1}$  with a 0.0025% average attenuation rate and only takes 87 s to charge fully. In conclusion, a heterogeneous interface provides active sites for  $\text{Na}^+$  and accelerates the movement rate of electron/ion; the hollow structure increases the contact area and alleviates the volume expansion. Therefore, (NiCu)S/NC electrode shows ultra-high capacity, outstanding rate performance, and excellent cycle stability as the anode for SIBs.

In order to analyze the storage mechanism of  $\text{Na}^+$  from a deeper perspective, we analyzed the reasons for its excellent rate performance through pseudo-capacitance analysis. Fig. 6(a–c) shows the CV profiles of (NiCu)S/NC, NiS/NC, and  $\text{Cu}_9\text{S}_5/\text{NC}$  at different scan rates from 0.5 to 2.5  $\text{mV s}^{-1}$ . The CV curves of (NiCu)S/NC keep a similar shape, indicating the high reversibility of electrochemical reaction. Due to the polarization, the redox peaks slightly shift with the increase in scan rate.  $\text{Na}^+$  storage mechanism can be qualitative analyzed according to the formula [58,59].

$$\log(i) = b \log(v) + \log(a) \quad (3)$$

Where  $i$  and  $v$  are adjustable parameters and the values of  $b$  are calculated by the logarithmic relationship between  $i$  and  $v$ . When the  $b$ -value tends to be 1, the  $\text{Na}^+$  storage mechanism is ascribed to the pseudo-capacitance. Alternatively, when the  $b$ -value is more inclined to 0.5, the storage mechanism of  $\text{Na}^+$  is controlled by bulk diffusion. By fitting two pairs of redox peaks in the CV curves of (NiCu)S/NC,  $b$ -values of Peak 1–4 are 0.88, 0.78, 0.60, and 0.81, suggesting that both diffusion controlled and capacitive  $\text{Na}^+$  storage mechanisms coexist in (NiCu)S/NC electrode (Fig. 6d). The fitting results of NiS/NC and  $\text{Cu}_9\text{S}_5/\text{NC}$  (Fig. 6e and f) also lead to the same conclusions. The following formula is used to quantify the ratio of pseudo-capacitance and bulk diffusion [24,60].

$$i(v) = k_1 v + k_2 v^{1/2} \quad (4)$$

Where  $k_1 v$  and  $k_2 v^{1/2}$  are on behalf of the pseudo-capacitance and bulk diffusion process, respectively. The specific proportions of (NiCu)S/NC, NiS/NC, and  $\text{Cu}_9\text{S}_5/\text{NC}$  are shown in Fig. 6(g–i), respectively. When the scan rate rises from 0.5 to  $2.5 \text{ mV s}^{-1}$ , the pseudo-capacitance contribution ratio of (NiCu)S/NC increases from 90.7% to 95.2%. By contrast, NiS/NC and  $\text{Cu}_9\text{S}_5/\text{NC}$  can only reach 82.3% and 88.7% at  $0.5 \text{ mV s}^{-1}$ . The better pseudo-capacitance diffusion ratio means more surface/near-surface sodium storage reaction, resulting in the stronger cyclic and rate performance. There are

three reasons for the formation of the high capacitance contribution: (1) hollow structure reduces ion/electron migration distance; (2) the formation of the built-in electric field accelerates the charge transfer; (3) the N-doped carbon in the (NiCu)S/NC matrix effectively improves the electrical conductivity.

Voltage platforms, CV curves, and XRD patterns of different states were conducted to confirm the reaction equations at different stages. The charge-discharge curves of (NiCu)S/NC, NiS/NC, and  $\text{Cu}_9\text{S}_5/\text{NC}$  are exhibited in Fig. 7(a), delivering the capacity of 395.7, 326.6, and  $221.2 \text{ mA h g}^{-1}$  at  $4 \text{ A g}^{-1}$  after 400 cycles. The charge-discharge platforms of NiS/NC and  $\text{Cu}_9\text{S}_5/\text{NC}$  are both presented in the compound of (NiCu)S/NC. The variation of voltage platforms (Fig. 7b) is obtained from the differential processing data of capacity-voltage in Fig. 7(a). Among these platforms, platform 2 in  $\text{Cu}_9\text{S}_5/\text{NC}$  and platform 3 in NiS/NC were merged into platform 1 in (NiCu)S/NC, and similar conditions were observed for peaks 4–6, 7–9, and 12–14. Platform 11 increases the capacity growth rate of (NiCu)S/NC. Fig. 7(c) shows the CV curves of (NiCu)S/NC, NiS/NC, and  $\text{Cu}_9\text{S}_5/\text{NC}$  at  $1 \text{ mV s}^{-1}$ . Due to the influence of polarization and the built-in electric field, the peak position is slightly shifted. These results manifest that NiS and  $\text{Cu}_9\text{S}_5$  have good compatibility in the electrochemical reaction, which means that the  $\text{Na}^+$  storage process of (NiCu)S/NC can be deduced through the  $\text{Na}^+$  storage process of NiS/NC and  $\text{Cu}_9\text{S}_5/\text{NC}$  in CV curves. Through literature review [61–63], the peak at 1.95 V represents the intercalation reaction of  $\text{Cu}_9\text{S}_5$  to  $\text{Na}_x\text{Cu}_9\text{S}_5$ . While the reduction peak at

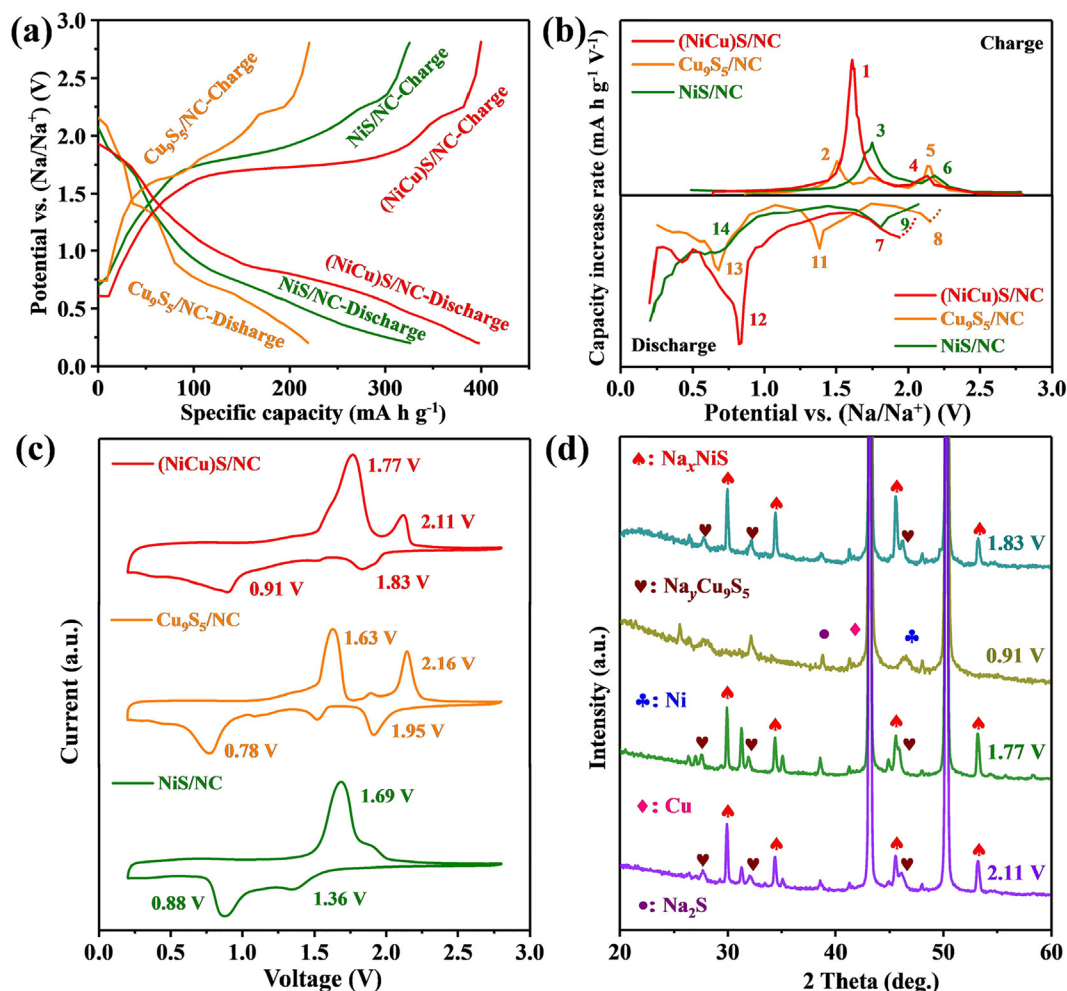


Fig. 7. Electrochemical  $\text{Na}^+$  storage process. (a) Charge-discharge curves and (b) capacity increase rates ( $d_{\text{capacity}}/d_v$ ) of (NiCu)S/NC, NiS/NC, and  $\text{Cu}_9\text{S}_5/\text{NC}$  at  $4 \text{ A g}^{-1}$ . (c) CV curves of (NiCu)S/NC, NiS/NC, and  $\text{Cu}_9\text{S}_5/\text{NC}$  at  $1 \text{ mV s}^{-1}$ . (d) Ex-situ XRD patterns of the (NiCu)S/NC at different charge/discharge states.

0.78 V corresponds to the converse reaction of  $\text{Na}_x\text{Cu}_9\text{S}_5$  to Cu and  $\text{Na}_2\text{S}$ . The oxidation peaks at 1.63 and 2.16 V are produced by the reverse reaction of Cu and  $\text{Na}_2\text{S}$ . For the electrochemical process of NiS, reduction peaks of 1.36 and 0.88 V originate from the intercalation ( $\text{NiS} \rightarrow \text{Na}_y\text{NiS}$ ) and converse reaction ( $\text{Na}_y\text{NiS} \rightarrow \text{Ni} + \text{Na}_2\text{S}$ ), respectively [64,65]. Therefore, the strong peak at 1.83 V in the CV curve of (NiCu)S/NC corresponds to the intercalation reaction ( $\text{Cu}_9\text{S}_5 \rightarrow \text{Na}_x\text{Cu}_9\text{S}_5$ ,  $\text{NiS} \rightarrow \text{Na}_y\text{NiS}$ ), and another reduction peak at 0.91 V is attributed to the reverse reaction ( $\text{Na}_x\text{Cu}_9\text{S}_5 \rightarrow \text{Cu} + \text{Na}_2\text{S}$ ,  $\text{Na}_y\text{NiS} \rightarrow \text{Ni} + \text{Na}_2\text{S}$ ). The formation of the peak at 1.77 V is due to the oxidations of Cu and Ni ( $\text{Cu} + \text{Na}_2\text{S} \rightarrow \text{Na}_x\text{Cu}_9\text{S}_5$ ,  $\text{Ni} + \text{Na}_2\text{S} \rightarrow \text{NiS}$ ). The last peak at 2.11 V is caused by the de-intercalation of  $\text{Na}^+$  ( $\text{Na}_x\text{Cu}_9\text{S}_5 + \text{Na}_2\text{S} \rightarrow \text{Cu}_9\text{S}_5$ ). The ex-situ XRD result also supports the reaction equations at different stages. When deep discharging to 0.91 V, the peaks of NiS and  $\text{Cu}_9\text{S}_5$  disappear with the appearance of Ni and Cu. The diffraction peaks of  $\text{Na}_x\text{NiS}$  and  $\text{Na}_y\text{Cu}_9\text{S}_5$  reappear at a charge state of 1.77 and 2.11 V. These results illustrate that NiS and  $\text{Cu}_9\text{S}_5$  in (NiCu)S/NC play the role of mutual reinforcement, leading to the improvement of the cyclic and rate capacity of the compound electrode.

$\text{Na}_3\text{V}_2(\text{PO}_4)_3/\text{C}$  (NVP/C) cathode was prepared to match the (NiCu)S/NC anode aiming to further prove potential application value of (NiCu)S/NC. NVP/C exhibits ultra-high reverse capacity of  $105.7 \text{ mA h g}^{-1}$  after 150 cycles at  $1 \text{ A g}^{-1}$  (Fig. 8a). As shown in Fig. 8(b), a pair redox peaks (3.22/3.52 V) can be observed in the CV profile of NVP/C, originating from the chemical reaction of  $\text{V}^{3+}/\text{V}^{4+}$ . The matched NVP/C cathode and (NiCu)S/NC anode are assembled into a full-battery (both anode and cathode materials are pre-cycled to form the stable SEI). The charge-discharge curve and cyclic performance of the full-battery are displayed in Fig. 8(c and d). The full-battery delivers a high capacity of  $288.7 \text{ mA h g}^{-1}$  after 50 cycles with a 93.7% retention rate. Similar to previous works by other researchers [66,67], the charging and discharging curves of (NiCu)S/NC- $\text{Na}_3\text{V}_2(\text{PO}_4)_3/\text{C}$  full-battery are very similar to those of NVP, which endows the full-battery with a high discharge voltage. Different from the NVP half-battery, the full-

battery has a slight voltage drop as the cycle increases. As shown in Fig. 8(e), (NiCu)S/NC delivers average capacities of 303.2, 296.3, 291.8, 280.4, and  $270.7 \text{ mA h g}^{-1}$ , when the current densities are 0.5, 0.8, 1.0, 1.2, and  $1.5 \text{ A g}^{-1}$ , respectively. And the reverse capacity recovers to  $289.8 \text{ mA h g}^{-1}$  with 99.3% capacity retention ratio, when the current density regains to  $1.0 \text{ A g}^{-1}$ . Such high capacity and excellent rate capability of (NiCu)S/NC- $\text{Na}_3\text{V}_2(\text{PO}_4)_3/\text{C}$  full-battery are attributed to excellent electrochemical performance and compatibility of the anode and cathode equally. The energy-power density (Ragone pots) is calculated according to the average discharge voltage, specific capacity, mass of active materials (the cathode/anode mass ratio is between 3.5 and 4), and discharge time data in Fig. 8(e). Ragone plots of (NiCu)S/NC- $\text{Na}_3\text{V}_2(\text{PO}_4)_3/\text{C}$  and other full-battery in the reported literatures are exhibited in Fig. 8(f) [26,68,69]. (NiCu)S/NC- $\text{Na}_3\text{V}_2(\text{PO}_4)_3/\text{C}$  full-battery exhibits ultra-high energy density of  $253.7 \text{ Wh kg}^{-1}$  at a power density of  $422.8 \text{ W kg}^{-1}$  (active material mass is the sum of the anode and cathode). Even at a power density of  $1293.6 \text{ W kg}^{-1}$ , the full-battery still delivers energy density of  $215.7 \text{ Wh kg}^{-1}$ .

To identify the essence of the enhanced electrochemical performance and obtain a better understanding of the effect of NiS- $\text{Cu}_9\text{S}_5$  heterojunction, several DFT calculations were performed to calculate the electronic properties of the heterojunction. The NiS crystal is well known as a good p-type semiconductor with a band gap of approximately 1.3 eV [34]. As for the  $\text{Cu}_9\text{S}_5$  crystal, it has been proven to possess excellent electrical conductivity, high mobility of copper ions, and high work function [33]. Thus it is a good candidate to be the electrode of SIBs. The comparison of the total density of states (TDOS) of NiS,  $\text{Cu}_9\text{S}_5$ , and NiS- $\text{Cu}_9\text{S}_5$  is displayed in Fig. 9(a and b). It is found that the new electronic state appears, leading to the vanishing of the band gap for the NiS- $\text{Cu}_9\text{S}_5$  heterojunction. This phenomenon delivers the increase in carrier concentration, which results in accelerated electron transfer and improved conductivity. In the meanwhile, we calculated the electrostatic potential of the heterojunction, as illustrated in Fig. 9(c).

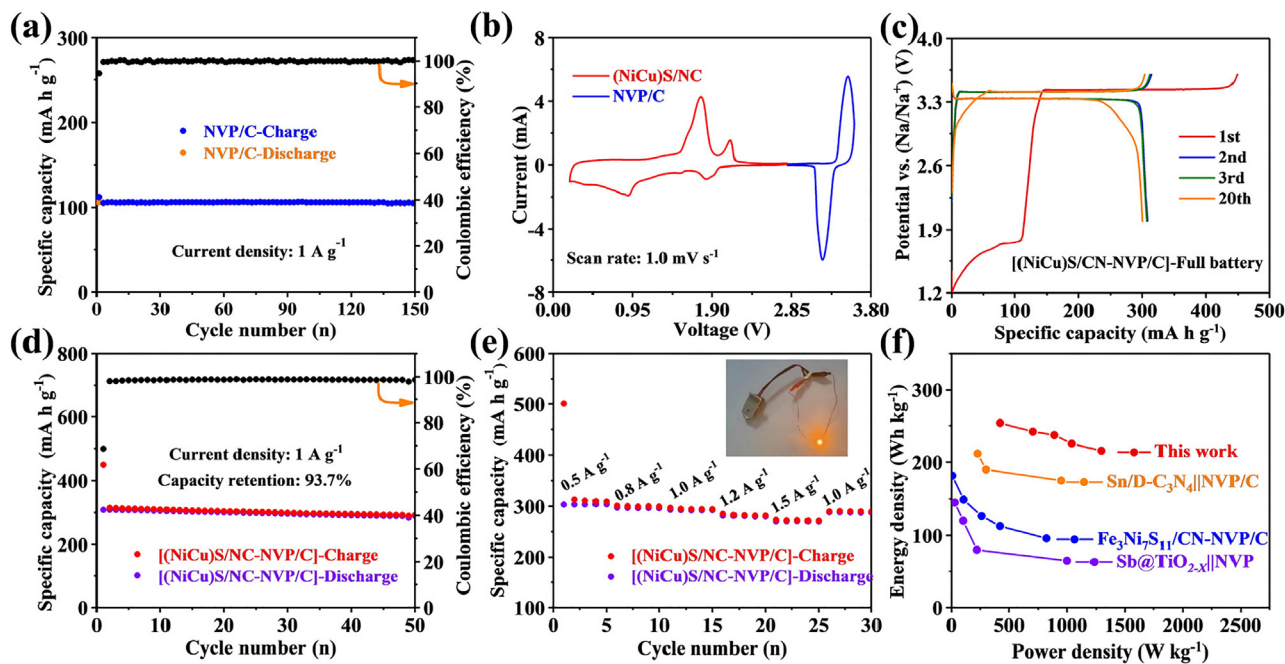


**Fig. 8.** Electrochemical properties for cathode and full-battery. (a) Cyclic performance of  $\text{Na}_3\text{V}_2(\text{PO}_4)_3/\text{C}$  at  $1 \text{ A g}^{-1}$ . (b) CV curves of (NiCu)S/NC and  $\text{Na}_3\text{V}_2(\text{PO}_4)_3/\text{C}$  at  $1 \text{ mV s}^{-1}$ . (c) Galvanostatic charge-discharge curves, (d) cyclic, and (e) rate performance of (NiCu)S/NC- $\text{Na}_3\text{V}_2(\text{PO}_4)_3/\text{C}$  full-battery. (f) The comparison of energy-power density (Ragone pots) between (NiCu)S/NC- $\text{Na}_3\text{V}_2(\text{PO}_4)_3/\text{C}$  and other full-battery.

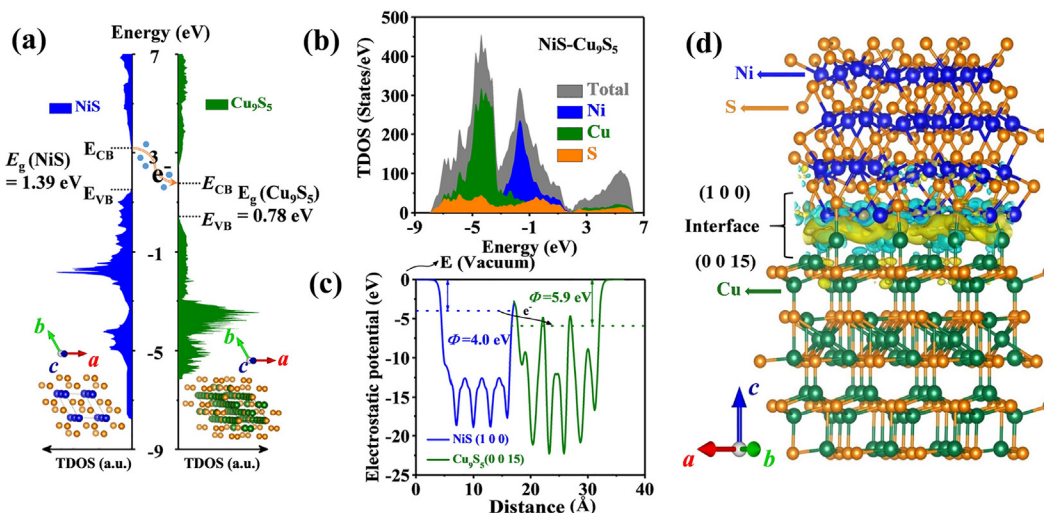


**Fig. 9.** TDOS of (a) NiS, Cu<sub>9</sub>S<sub>5</sub>, and (b) NiS-Cu<sub>9</sub>S<sub>5</sub>. (c) Calculated electrostatic potential of heterojunction (the NiS (1 0 0) and Cu<sub>9</sub>S<sub>5</sub> (0 0 15) surface are depicted by blue and green lines, respectively). (d) 3D real space differential charge distribution of the interface of NiS-Cu<sub>9</sub>S<sub>5</sub>. Cyan and yellow denote charge reduction and accumulation, respectively.

The work function of NiS (1 0 0) surface is 4.0 eV, which is much lower than that of Cu<sub>9</sub>S<sub>5</sub> (0 0 15) surface. Therefore, when the NiS-Cu<sub>9</sub>S<sub>5</sub> heterojunction is successfully formed, electrons will flow from the NiS surface with a higher Fermi level to the Cu<sub>9</sub>S<sub>5</sub> surface with a lower Fermi level, resulting in the formation of built-in electric fields. These can also be proven by the three-dimensional (3D) differential charge distribution, as plotted in Fig. 9(d). The electrons accumulated in the interface and wrapped around the Cu atoms. The charges flow from Ni to the heterojunction and Cu atoms, which verify the formation of built-in electric field and the highly promoted electrochemical properties. In summary, compared to the Cu<sub>9</sub>S<sub>5</sub> and NiS crystal, NiS-Cu<sub>9</sub>S<sub>5</sub> heterojunction will increase the carrier concentration by forming the built-in electric field, thereby accelerating the charge transfer and enhancing the electrochemical performance.

#### 4. Conclusions

In summary, hollow hetero-sphere of (NiCu)S/NC was synthesized successively through one-step solvo-thermal and carbonization treatment. As an anode for SIBs, (NiCu)S/NC delivers high reverse capacity (559.2 mA h g<sup>-1</sup> at 0.5 A g<sup>-1</sup> for the second cycle), excellent rate capability (185.3 mA h g<sup>-1</sup> at the high current density of 15 A g<sup>-1</sup>), and long-durable stability (342.6 mA h g<sup>-1</sup> at 4 A g<sup>-1</sup> after 1500 cycles, 150.0 mA h g<sup>-1</sup> at 10 A g<sup>-1</sup> after 20,000 cycles). Furthermore, (NiCu)S/NC-Na<sub>3</sub>V<sub>2</sub>(PO<sub>4</sub>)<sub>3</sub>/C full-battery shows high energy density (253.7 W h kg<sup>-1</sup>) and reverse capacity (288.7 mA h g<sup>-1</sup>). Compared with the electrochemical performance of NiS/NC and Cu<sub>9</sub>S<sub>5</sub>/NC, the significant improvement of sodium storage capacity of (NiCu)S/NC originates from the formation of heterogeneous interfaces and increase of effective active area. Additionally, the enhancement of rate capacity is beneficial to the increase in electrical conductivity, originating from the formation of built-in electric field and high-proportioned pseudocapacitance. The design of hollow structure and optimization of the sodium storage mechanisms reinforce the structural stability of (NiCu)S/NC during the cycling process. DFT calculations prove that NiS-Cu<sub>9</sub>S<sub>5</sub> heterojunction will increase the carrier concentration by forming the built-in electric field. Consequently, the unique hollow sphere of heterojunction (NiCu)S/NC can be a promising candidate as the advanced anode for SIBs.

#### Declaration of competing interest

The authors declare that they have no known competing financial interests or personal relationships that could have appeared to influence the work reported in this paper.

#### Acknowledgments

This work was financial supported by the National Natural Science Foundation of China (51572202), the National Nature Science Foundation of Jiangsu Province (BK20221259) and Duozhu Technology (Wuhan) Co., Ltd. We thank the Core Facility of Wuhan University for characteristic analysis.

#### Appendix A. Supplementary data

Supplementary data to this article can be found online at <https://doi.org/10.1016/j.jechem.2023.03.018>.

#### References

- [1] T.C. Liu, J.J. Liu, L.X. Li, L. Yu, J.C. Diao, T. Zhou, S.N. Li, A. Dai, W.G. Zhao, S.Y. Xu, Y. Ren, L.G. Wang, T.P. Wu, R. Qi, Y.G. Xiao, J.X. Zheng, W. Cha, R. Harder, I. Robinson, J.G. Wen, J. Lu, F. Pan, K. Amine, Nature 606 (2022) 305–312.
- [2] Y.L. Jiang, H. Wang, J. Dong, Q.X. Zhang, S.S. Tan, F.Y. Xiong, W. Yang, S.H. Zhu, Y.H. Shen, Q.L. Wei, Q.Y. An, L.Q. Mai, Small 18 (2022) 2200805.
- [3] H.Z. Liu, J.H. Li, X.N. Zhang, X.X. Liu, Y. Yan, F.J. Chen, G.H. Zhang, H.G. Duan, Adv. Funct. Mater. 31 (2021) 2106550.
- [4] T.W. Chen, Z.W. Shuang, J. Hu, Y.L. Zhao, D.H. Wei, J.H. Ye, G.H. Zhang, H.G. Duan, Small 18 (2022) 2201628.
- [5] G.H. Zhang, X.J. Li, D.H. Wei, H.H. Yu, J.H. Ye, S. Chen, W. Zhang, J. Zhu, X.D. Duan, Chem. Eng. J. 453 (2023).
- [6] J.M. Tarascon, M. Armand, Nature 414 (2001) 359–367.
- [7] X.W. Liu, X.H. Shen, H. Li, P. Li, L.B. Luo, H.M. Fan, X.M. Feng, W.H. Chen, X.P. Ai, H.X. Yang, Y.L. Cao, Adv. Energy Mater. 11 (2021) 2003905.
- [8] S.Y. Hong, Y. Kim, Y. Park, A. Choi, N.S. Choi, K.T. Lee, Environ. Sci. 6 (2013) 2067–2081.
- [9] C.L. Zhao, Q.D. Wang, Z.P. Yao, J.L. Wang, B. Sanchez-Lengeling, F.X. Ding, X.G. Qi, Y.X. Lu, X.D. Bai, B.H. Li, H. Li, A. Aspuru-Guzik, X.J. Huang, C. Delmas, M. Wagemaker, L.Q. Chen, Y.S. Hu, Science 370 (2020) 708.
- [10] X.Y. Li, K.K. Li, S.C. Zhu, K. Fan, L.L. Lyu, H.M. Yao, Y.Y. Li, J.L. Hu, H.T. Huang, Y. W. Mai, J.B. Goodenough, Angew. Chem. Int. Ed. 58 (2019) 6239–6243.
- [11] X.M. Lin, X.T. Yang, H.N. Chen, Y.L. Deng, W.H. Chen, J.C. Dong, Y.M. Wei, J.F. Li, J. Energy Chem. 76 (2023) 146–164.
- [12] X. Wu, X.Y. Xiong, B. Yuan, J. Liu, R.Z. Hu, J. Energy Chem. 72 (2022) 133–142.
- [13] D.G. Sun, C. Tang, H. Cheng, W.L. Xu, A.J. Du, H.J. Zhang, J. Energy Chem. 72 (2022) 1–8.
- [14] X.Y. Wu, Z.S. Yang, L. Xu, J.H. Wang, L.L. Fan, F.J. Kong, Q.F. Shi, Y.Z. Piao, G.W. Diao, M. Chen, J. Energy Chem. 74 (2022) 8–17.

- [15] Y.Q. Li, Q. Zhou, S.T. Weng, F.X. Ding, X.G. Qi, J.Z. Lu, Y. Li, X. Zhang, X.H. Rong, Y. X. Lu, X.F. Wang, R.J. Xiao, H. Li, X.J. Huang, L.Q. Chen, Y.S. Hu, *Nat. Energy* 7 (2022) 511–519.
- [16] D. Cao, W. Kang, W. Wang, K. Sun, Y. Wang, P. Ma, D. Sun, *Small* 16 (2020) 1907641.
- [17] K. Zhang, M. Park, L. Zhou, G.-H. Lee, J. Shin, Z. Hu, S.-L. Chou, J. Chen, Y.-M. Kang, *Angew. Chem. Int. Ed.* 55 (2016) 12822–12826.
- [18] S. Huang, Y. Li, S. Chen, Y. Wang, Z. Wang, S. Fan, D. Zhang, H.Y. Yang, *Energy Storage Mater.* 32 (2020) 151–158.
- [19] J.Y. Zhang, Z. Meng, D. Yang, K.M. Song, L.W. Mi, Y.P. Zhai, X.X. Guan, W.H. Chen, *J. Energy Chem.* 68 (2022) 27–34.
- [20] D. Lv, D.D. Wang, N.N. Wang, H.X. Liu, S.J. Zhang, Y.S. Zhu, K.P. Song, J. Yang, Y. T. Qian, *J. Energy Chem.* 68 (2022) 104–112.
- [21] W.L. Feng, V.S. Avvaru, S.J. Hinder, V. Etacheri, *J. Energy Chem.* 69 (2022) 338–346.
- [22] Z. Hu, Z.Q. Zhu, F.Y. Cheng, K. Zhang, J.B. Wang, C.C. Chen, J. Chen, *Energy Environ. Sci.* 8 (2015) 1309–1316.
- [23] W.X. Zhao, C.X. Guo, C.M. Li, *J. Mater. Chem. A* 5 (2017) 19195–19202.
- [24] H.Y. Chen, S.Y. Wan, P.F. Tian, Q.M. Liu, *A.C.S. Appl. Energy Mater.* 4 (2021) 12728–12737.
- [25] L.K. Fu, W.Q. Xiong, Q.M. Liu, S.Y. Wan, C.X. Kang, G.F. Li, J. Chu, Y.C. Chen, S.J. Yuan, *J. Alloys Compd.* 869 (2021).
- [26] H.Y. Chen, P.F. Tian, L.K. Fu, S.Y. Wan, Q.M. Liu, *Chem. Eng. J.* 430 (2022).
- [27] H.L. Long, X.P. Yin, X. Wang, Y.F. Zhao, L.M. Yan, *J. Energy Chem.* 67 (2022) 787–796.
- [28] S. Fan, S.Z. Huang, Y.X. Chen, Y. Shang, Y. Wang, D.Z. Kong, M.E. Pam, L.L. Shi, Y. W. Lim, Y.M. Shi, H.Y. Yang, *Energy Storage Mater.* 23 (2019) 17–24.
- [29] D. Yuan, Y.H. Dou, Y.H. Tian, D. Adekoya, L. Xu, S.Q. Zhang, *Angew. Chem. Int. Ed.* 60 (2021) 18830–18837.
- [30] P. Du, L. Cao, B. Zhang, C.H. Wang, Z.M. Xiao, J.F. Zhang, D. Wang, X. Ou, *Renew. Sustain. Energy Rev.* 151 (2021).
- [31] H.Q. Xie, M. Chen, L.M. Wu, *A.C.S. Appl. Mater. Interfaces* 11 (2019) 41222–41228.
- [32] S.A. He, Z. Cui, Q. Liu, G.J. He, D.J.L. Brett, W. Luo, R.J. Zou, M.F. Zhu, *Small* 17 (2021) 2104186.
- [33] Z. Peng, S.B. Li, M.Y. Weng, M.J. Zhang, C. Xin, Z. Du, J.X. Zheng, F. Pan, *J. Phys. Chem. C* 121 (2017) 23317–23323.
- [34] J.H. Lee, S.I. Kim, S.M. Park, M. Kang, *Ceram. Int.* 43 (2017) 1768–1774.
- [35] H.Y. Chen, X.T. Yang, P.F. Lv, P.F. Tian, S.Y. Wan, Q.M. Liu, *Chem. Eng. J.* 450 (2022).
- [36] P.E. Blochl, *Phys. Rev. B* 50 (1994) 17953–17979.
- [37] G. Kresse, J. Furthmuller, *Phys. Rev. B* 54 (1996) 11169–11186.
- [38] D. Chakraborty, K. Berland, T. Thonhauser, *J. Chem. Theory Comput.* 16 (2020) 5893–5911.
- [39] H.J. Monkhorst, J.D. Pack, *Phys. Rev. B* 13 (1976) 5188.
- [40] S.J. Guan, Q.L. Fan, Z.C. Shen, Y.L. Zhao, Y. Sun, Z.C. Shi, *J. Mater. Chem. A* 9 (2021) 5720–5729.
- [41] X.X. Yu, L. Wang, H. Yin, *Appl. Mater. Today* 15 (2019) 582–589.
- [42] J.B. Li, J.L. Li, D. Yan, S.J. Hou, X.T. Xu, T. Lu, Y.F. Yao, W.J. Mai, L.K. Pan, *J. Mater. Chem. A* 6 (2018) 6595–6605.
- [43] C.B. Zhou, S.Y. Wan, Y.C. Chen, L.K. Fu, H.Y. Chen, C.X. Kang, Q.M. Liu, *J. Power Sources* 509 (2021).
- [44] Y. Jiang, F. Wu, Z.Q. Ye, Y.Z. Zhou, Y. Chen, Y.X. Zhang, Z.K. Lv, L. Li, M. Xie, R.J. Chen, *Chem. Eng. J.* 451 (2023).
- [45] C.C. Liu, Q.Q. Lu, M.V. Gorbunov, A. Omar, I.G. Gonzalez Martinez, P.P. Zhao, M. Hantusch, A. Dimas Chandra Permana, H. He, N. Gaponik, D. Mikhailova, *J. Energy Chem.* 79 (2023) 373–381.
- [46] M.J. Jing, F.Y. Li, M.J. Chen, J.H. Zhang, F.L. Long, L.M. Jing, X.P. Lv, X.B. Ji, T.J. Wu, *J. Alloys Compd.* 762 (2018) 473–479.
- [47] Z.H. Zeng, S.H. Yuan, C.X. Yi, W.Q. Zhao, Z.Q. Yuan, Y. Dong, J.L. Zhu, Y. Yang, P. Ge, *A.C.S. Appl. Mater. Interfaces* 14 (2022) 52067–52078.
- [48] S.Y. Wan, X. Liu, L.K. Fu, C.B. Zhou, H.Y. Chen, G.H. Li, S.Y. Cao, Q.M. Liu, *J. Alloys Compd.* 870 (2021).
- [49] S.Y. Wan, Q.M. Liu, M. Cheng, Y.C. Chen, H.Y. Chen, *A.C.S. Appl. Mater. Interfaces* 13 (2021) 38278–38288.
- [50] S.Y. Wan, M. Cheng, H.Y. Chen, H.J. Zhu, Q.M. Liu, *J. Colloid Interface Sci.* 609 (2022) 403–413.
- [51] Q. Liu, S.J. Zhang, C.C. Xiang, C.X. Luo, P.F. Zhang, C.G. Shi, Y. Zhou, J.T. Li, L. Huang, S.G. Sun, *A.C.S. Appl. Mater. Interfaces* 12 (2020) 43624–43633.
- [52] Y.H. Zhang, C.X. Lv, X. Wang, S. Chen, D.H. Li, Z. Peng, D.J. Yang, *A.C.S. Appl. Mater. Interfaces* 10 (2018) 40531–40539.
- [53] J.H. Huang, Y.S. Yao, M. Huang, Y.F. Zhang, Y.F. Xie, M.L. Li, L.L. Yang, X.L. Wei, Z. W. Li, *Small* 18 (2022) 2200782.
- [54] H.Y. Wu, N. Xu, Z.H. Jiang, A.Y. Zheng, Q.F. Shi, R.G. Lv, L.B. Ni, G.W. Diao, M. Chen, *Chem. Eng. J.* 427 (2022).
- [55] S.G. Zhang, G.Y. Yin, H.P. Zhao, J. Mi, J. Sun, L.Y. Dang, *J. Mater. Chem. C* 9 (2021) 2933–2943.
- [56] B. Yu, Y. Ji, X. Hu, Y. Liu, J. Yuan, S. Lei, G. Zhong, Z. Weng, H. Zhan, Z. Wen, *Chem. Eng. J.* 430 (2022).
- [57] Y.J. Fang, D.Y. Luan, Y. Chen, S.Y. Gao, X.W. Lou, *Angew. Chem. Int. Ed.* 59 (2020) 7178–7183.
- [58] L.K. Fu, C.X. Kang, W.Q. Xiong, P.F. Tian, S.Y. Cao, S.Y. Wan, H.Y. Chen, C.B. Zhou, Q.M. Liu, *J. Colloid Interface Sci.* 595 (2021) 59–68.
- [59] J. Rahmatinejad, X.D. Liu, X.M. Zhang, B. Raisi, Z.B. Ye, *J. Energy Chem.* 75 (2022) 240–249.
- [60] X.Q. Ma, Y.D. Li, X.J. Long, H.C. Luo, C.P. Xu, G.Z. Wang, W.X. Zhao, *J. Energy Chem.* 77 (2023) 227–238.
- [61] H. Park, J. Kwon, H. Choi, D. Shin, T. Song, X.W. Lou, *ACS Nano* 12 (2018) 2827–2837.
- [62] Y.J. Fang, X.Y. Yu, X.W. Lou, *Angew. Chem. Int. Ed.* 58 (2019) 7744–7748.
- [63] X.Q. Liu, X.Y. Li, X.L. Lu, X. He, N. Jiang, Y. Huo, C.G. Xu, D.M. Lin, *J. Alloys Compd.* 854 (2021).
- [64] D. Zhang, W.P. Sun, Y. Zhang, Y.H. Dou, Y.Z. Jiang, S.X. Dou, *Adv. Funct. Mater.* 26 (2016) 7479–7485.
- [65] M.K. Sadan, H. Kim, C. Kim, G.B. Cho, K.K. Cho, J.H. Ahn, H.J. Ahn, *Nanoscale* 13 (2021) 10447–10454.
- [66] B.H. Hou, Y.Y. Wang, J.Z. Guo, Q.L. Ning, X.T. Xi, W.L. Pang, A.M. Cao, X.L. Wang, J.P. Zhang, X.L. Wu, *Nanoscale* 10 (2018) 9218–9225.
- [67] Z.Y. Gu, J.Z. Guo, Z.H. Sun, X.X. Zhao, W.H. Li, X. Yang, H.J. Liang, C.D. Zhao, X.L. Wu, *Sci. Bull.* 65 (2020) 702–710.
- [68] N.N. Wang, Z.C. Bai, Y.T. Qian, J. Yang, *Adv. Mater.* 28 (2016) 4126–4133.
- [69] J.S. Lee, R. Saroha, J.S. Cho, *Nano-Micro Lett.* 14 (2022) 113.